Visualization experiments of a solid cylinder suspended by laminar flow

Weidong Guo [a,b], Yujie Wu [a,b], Chao Wang [a,b], Hao Chen [a,b], Zhipeng Li [a,b,*], Zhengming Gao [a,b,*], J.J. Derksen [c]

[a] Beijing Advanced Innovation Center for Soft Matter Science and Engineering, Beijing University of Chemical Technology, Beijing 100029, China

[b] State Key Laboratory of Chemical Resource Engineering, School of Chemical Engineering, Beijing University of Chemical Technology, Beijing 100029, China

[c] School of Engineering, University of Aberdeen, Aberdeen AB24 3UE, UK

[*] Corresponding author. Tel.: +8610 64418267; fax: +8610 64449862. E-mail address: lizp@buct.edu.cn (Zhipeng Li), gaozm@buct.edu.cn (Zhengming Gao).

Abstract

The suspension of a single cylindrical particle in a square stirred tank was investigated by detailed visualization experiments. The flow pattern in the tank generated by a spinning disk is laminar (Reynolds numbers based on the disk diameter are less than 50). The cylinder's motion and orientation were recorded by two cameras at 100 frames per second and then quantitatively analyzed. The length over diameter aspect ratio of the cylinders was varied in the range $1 - 8$. The angular speed of the spinning disk at which incipient lift-off of the cylinder occurs depends on the cylinder's diameter and its aspect ratio. Beyond an aspect ratio of about 5, this critical disk speed only weakly depends on the aspect ratio indicating that then the hydrodynamic force on the cylinder approximately scales with its length. The self-rolling as well as the azimuth sliding over the tank bottom were quantitatively identified when the cylinder approached being lifted off. The suspension phenomenon of the cylinder with aspect ratio 1 is different from other cylinders. We obtained highly reproducible results for the trajectory and orientation of the cylinder during the suspension process that can serve as benchmark data for critical evaluation of computational approaches.

Keywords: Solid-liquid suspension; stirred tank; cylindrical particle; laminar flow; orientation

1. Introduction

Entrainment of solid particles in a liquid stream is a common phenomenon in nature and in engineered systems such as sediment transport in rivers, dredging pipelines transporting slurry, heterogeneous liquid-phase reactions on solid catalyst surfaces, and crystallization processes in agitated reactors.

In agitated tanks, suspending solids in a liquid phase increases the contact area of the two phases which enhances mass transfer. Therefore, determining critical conditions for solids suspension is significant for the design and operation of stirred tanks: near critical conditions, most of the solids are suspended with minimum power input. Many studies have been carried out to determine the critical suspension conditions. Zwietering (Zwietering, 1958) proposed the concept of just suspended speed N_{js} and established a widely-used correlation for N_{js} including many factors such as size of the vessel, type of the stirrer and density and size of the solids. Many researchers (Baldi et al., 1978; Jafari et al., 2012; N. Sharma and A. Shaikh, 2003) have extended Zwietering's work and established just-suspended correlations for different geometrical and

operating conditions.

In previous work (Mo et al., 2015; Wang et al., 2018), we studied suspension processes of spherical particles in mixing tanks at a fundamental level. Focusing on mechanisms of single-particle suspension, Mo et al. (Mo et al., 2015) combined experiments and simulations to study a single spherical particle in a stirred tank and the way it is entrained by the fluid flow. The motion of the sphere was quantitatively visualized in detail. For the specific conditions studied, the scaling of the suspending force with the impeller speed was intermediate between viscous and inertial scaling. The simulated results based on the lattice-Boltzmann method (LBM) agreed with experimental data within a 3% uncertainty. Wang et al. (Wang et al., 2018) studied multi-spheres suspension in laminar stirred tank flow. They found stable patterns of particles obstructing the suspension process. The pressure gradient around spheres on or close to the bottom wall plays an important role during the lift-off process.

Different from the above situations, solid particles in many processes do not have a spherical shape. For example, the shape of rough wrought biomass particles is generally irregular, often fibrous, and clearly non-spherical. Such particles are often present in the conversion process of biomass energy in the stirred reactor (Zheng et al., 2019). Biomass had been recognized as a promising resource for future energy(Pang, 2019).

Many researchers have focused on the motion of non-spherical particles through liquid. Extensive experimental works about the settling of irregular particles have been conducted. They investigated the terminal settling velocity, drag coefficient and orientation of particles (Haider and Levenspiel, 1989; Tran-Cong et al., 2004). Liu and Joseph (Liu and Joseph, 1993) studied long cylinders falling in viscoelastic liquids. They measured the tilt angles of cylinders while settling and found that its angle with the horizontal varies from 0° (inertia dominated) to 90° (viscoelasticity dominated). Turney et al.(Turney et al., 1995) used Magnetic Resonance Imaging (MRI) to experimentally study fiber suspensions and obtained a correlation between terminal settling velocity and aspect ratio. Furthermore, some researchers explored the wall effect on the settling of cylindrical particles and established an empirical model (Lau et al., 2010; Unnikrishnan and Chhabra, 1991). Chhabra et al. (Chhabra et al., 1999) collected experimental data about settling particles including cylinders, prisms, discs, and cubes. The particles' sphericity ranged from 0.09 to 1 and the flow varied from creeping flow to turbulent flow. They evaluated some widely used correlations for estimating the drag coefficient of non-spherical particles. There are also many computational works about non-spherical particles (Derksen, 2019; Derksen, 2020; Qi, 2001; Salmela et al., 2007). Most of these studies have shown that non-spherical particles exhibit

preferential orientation while falling through a quiescent fluid (Fan et al., 2004; Jianzhong et al., 2003).

Recently the suspension with non-spherical particles in agitated systems attracted many researchers' attention. Fan et al. (Fan and Xu, 2017a, b) experimentally studied fiber particles in a baffled tank stirred with a standard six-blade Rushton turbine in the laminar and turbulent regime. Digital Particle Image Velocimetry (DPIV) was used to identify the influence of impeller speed, fiber aspect ratio and solids concentration on the velocity field and the orientation of fibers. Comparing the velocity distribution of fiber particles with spherical particles, they found that the particle's shape has an influence on the particle and fluid velocity variation over space in laminar flow. Derksen (Derksen, 2020) simulated the critical suspension and orientation of cylindrical particles in three-dimensional laminar flow. The overall solids volume fraction was 15% (the number of cylinders was of the order of one thousand). The aspect ratio of the cylinders ranges from 1 to 4. The simulated results show that the cylindrical particles with a larger aspect ratio are easier to be suspended.

While the above studies involve the collective behavior of non-spherical particle suspensions, in order to fundamentally (at the particle scale) understand the suspension phenomenon of cylindrical particles and establish experimental validation for numerical method, the current paper focuses on a single cylindrical particle and the way it is entrained by liquid flow. In addition, we choose the flow condition in the stirred tank as laminar. By simplifying the flow field, we will focus on the physical mechanism that drives cylinder lift-off. Our first aim is to determine the critical conditions to lift off a single cylinder in a stirred tank and investigate the influence of the diameter and aspect ratio on the cylinder's incipient vertical motion. The second aim is to develop reliable and reproducible image detection and analysis based on a two-camera system to measure the centroid and the orientation of the cylinder during suspension so that its motion can be quantified. The third aim is to compare the motion and orientation of cylinders over a range of aspect ratios qualitatively and quantitatively. The overarching aim is to generate an experimental data set that can be built upon when extending our experimental work to multi-cylinder systems and can be used for validating numerical simulation procedures involving non-spherical particles in fluid flow.

The paper is organized as follows: the experimental setup including apparatus geometry, liquid conditions, and particle properties are described first. Next, experimental methods, quantitative visualization of cylinder motion as well as the criterion for determining critical conditions are introduced. In the results and discussion section, first the critical impeller speeds as a function of

cylinder diameter and aspect ratio are presented and interpreted. Then, quantitative information about cylinder motion (trajectory and orientation) is discussed, with an emphasis on reproducibility of the experiments and the linear offset distance model of the cylindrical particle before it is suspended. The final section reiterates the main conclusions and puts forward future research.

2. Experiment setup

2.1. Flow system

The experiments were conducted in a square, flat-bottomed tank in order to have better optical access for understanding solids suspension mechanism, and the flow was agitated by using a rotating disk. The geometry of the tank and the disk, as well as the Cartesian coordinates, are shown in Fig. 1 (a). The side length of the tank is $T = 0.220$ m, and the liquid height inside the tank is $H = T$. The diameter of the disk is $D = 0.5T$, and its off-bottom clearance is $C = 0.25T$. The origin of the Cartesian coordinate system is at the bottom center of the tank.
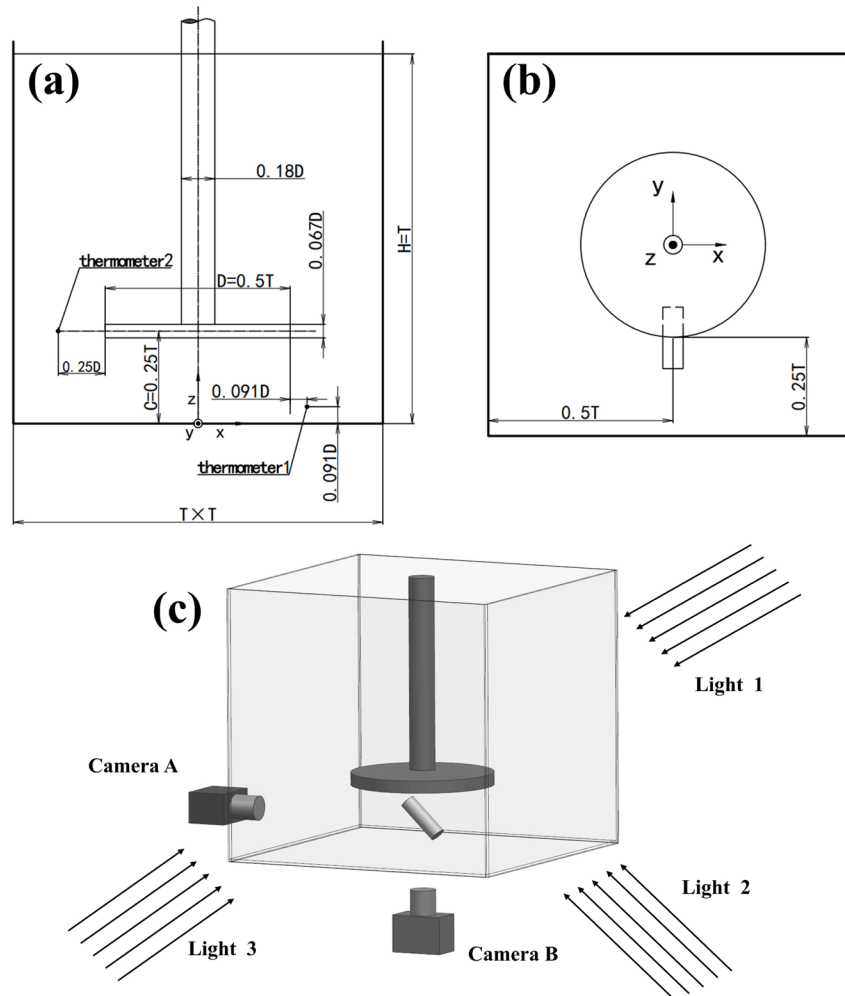

Fig. 1 - (a) Stirred tank geometry: a circular disk spins in a square tank with side length $T = 0.220$

m, definition of the Cartesian coordinate system, and location of temperature measurements. (b) The initial position of the solid cylinder. (c) Layout of visualization the experiments with camera A capturing the side view and camera B capturing the bottom view.

Dimethyl silicone oil (supplied from Shanghai Lubao Company) was chosen as the working liquid because of its stability and transparency. The dynamic viscosity of the liquid was measured by a MARS40 Rheometer (Haake, Germany). The correlation between the dynamic viscosity μ (in Pa·s) and mean temperature T_m (in °C) is $\mu = 2.8573 - 0.03533 T_m$. At the start and the end of each experiment we measured the temperature of the liquid at two locations that are indicated in Fig. 1 (a). The mean temperature in each experiment was the average of the four measured temperatures, and it was controlled at 25.2±0.1 °C by using air conditioning. With temperature fluctuating about ±0.1 °C, the variation of the dynamic viscosity is no more than 0.2%. The density of the dimethyl silicone oil is $\rho = 965$ kg/m^3.

PTFE (Poly tetra fluoroethylene) cylinders with five diameters d and various lengths l were used in the experiments (see Table S1 in the appendix). The aspect ratio l/d of the cylinders used for determining critical lift-off condition ranges from approximately 1 to 8. The density ratio of the cylinders and the silicone oil is $\rho_p/\rho = 2.28$.

We aim to quantify critical conditions for the cylinders being suspended. We defined the critical lift-off speed N_{LO} (in revolutions per second) as the lowest rotational speed of the disk so that the cylinder could be lifted off the tank bottom within 60 s (in the next sub-section it is explained when the clock is started). The uncertainty of the N_{LO} in our experiments is less than 1.0%. For example, the N_{LO} for the cylinder with $d = 12.00$ mm and $l/d = 3.00$ is 410 rpm, as shown in Table S1. If we decrease the rotational speed by around 1% to 407 rpm, the cylinder is not lifted off within 60 s. Each experiment was repeated at least three times.

In this study, we used several dimensionless numbers. The Reynolds number in the agitated tank is defined as $Re = \frac{ND^2}{v}$ with v the kinematic viscosity of the liquid (in m^2/s). The highest Reynolds number is less than 50, which means the flow in the tank is laminar (Lamberto et al., 1999; Takahashi et al., 2012; Zalc et al., 2001). The viscous Shields number accounts for the presence of cylinders in the flow. Given the non-spherical shape of the particles used, the viscous Shields number is based on their volume V and surface area S: $\theta = \frac{\mu NS}{g(\rho_p - \rho)V}$, where g is the gravitational acceleration (in m/s^2). The Shields number indicates the ratio of viscous force suspending the cylinder to net gravity force pulling the particle down.

2.2. Visualization experiment and image processing

Our experimental procedure was as follows: a cylindrical particle was initially placed at the bottom of the tank with particle center location $(x, y, z) = (0.0, -0.5D, 0.5d)$, which is shown in Fig. 1 (b). We determined the first estimate for the target speed with a constant acceleration of 100 revolution/minute/s (rpm/s). If the cylinder could not be lifted off within 60 seconds starting from the moment the disk started to rotate we increased the target speed by less than 1% and repeated the experiment from scratch. The critical lift-off speed N_{LO} was achieved until the cylinder could be lifted off within 60 seconds, and the uncertainty of the N_{LO} was less than 1%. Our previous research reports that laminar flow reaches steady state very shortly after the end of accelerating process of the impeller (Mo et al., 2015). When the cylindrical particle was lifted off, the overall flow field in the tank had already reached steady state. Therefore, the acceleration process doesn't affect the cylinder's suspension.

Two high-speed cameras (Dantec Dynamics A/S, Denmark) were used to monitor the motion of the cylinder, as illustrated in Fig. 1 (c). Camera A was set near the side wall of the tank and captured the vertical motion of the cylinder. Camera B was underneath the tank and captured the motion of the cylinder in the horizontal plane. The cylinders were painted white, and strong lights were used to make the captured images sharp and contrast-rich. A resolution 1280×1024 pixel^2 with 0.15 and 0.14 mm per pixel for side and bottom respectively and a capture frequency of 100 frames per second (fps) were used. Representative raw images in side and bottom view are shown in Fig. 2 (a) and Fig. 2 (b).

The raw images were processed and analyzed in a Matlab environment (version: R2022a, MathWorks, USA) to capture the movement information of the cylinder. First, the raw image was pre-processed via binarization and mathematical morphology operations (van den Boomgaard and van Balen, 1992) to obtain the binary image of the cylinder and wipe off interference. Then, the Matlab function *bwlabel* (Haralick and Shapiro, 1992) and *regionprops* (Zhang and Yu, 2017) were employed to find the center location and calculate the orientation of the cylinder. The *bwlabel* function returned a matrix that contains labels for the 8-connected objects found in the above pre-processed binary image. Next, the *regionprops* function returned the values of properties specified for each 8-connected object in the binary image. Finally, the so obtained data can be used to calculate the cylinder's centroid and orientation. The image processing procedure has been illustrated in Figs. 2 (c), 2 (d) and 2 (e). As one can see, the cylinder's outline, center location, and deflection direction are displayed accurately. The detection is fully automatic.

However, there are some raw frames where the contrast between the cylinder and the background is weak so that cylinder's details are lost and the Matlab code could not process the images correctly. In these cases, manual operation to enhance image contrast is necessary.
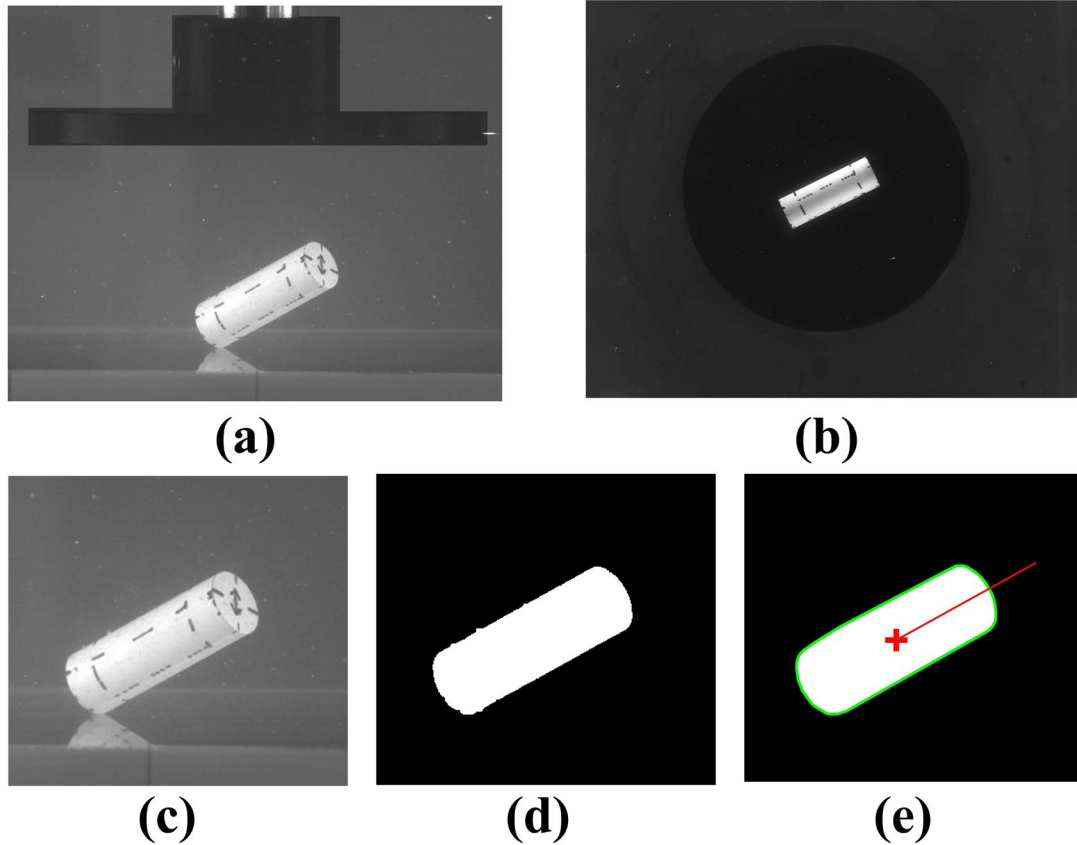

(a) **(b)**

(c) **(d)** **(e)**

Fig. 2 - Sample frames: (a) the cylinder rising toward the disk (Camera A); (b) the cylinder rotating over the bottom (Camera B). Image processing steps in detection of the cylinder position: (c) raw camera frame; (d) image after binarization; (e) detection of particle position. The particle's profile (green curve), center (red cross) and axis (red line) as indicated.

The orientation of cylindrical particles is an important characteristic. Qi et al. (Qi et al., 2014; Qi et al., 2012) presented a measurement method to obtain the orientation of fibrous particles while settling in air. They employed a two-dimensional particle tracking velocimetry (PTV) system to capture the particle's motion and calculated the fiber's orientation based on the coordinates of its end-points. Krueger et al. (Krueger et al., 2015) presented a novel experimental set-up based on a drop shaft armed with two digital cameras which automatically obtained the motion information of irregular particle and determined the orientation of the particle. Chen et al. (Chen et al., 2019) used X-ray particle tracking velocimetry (XPTV) to obtain the motion information of a cylindrical particle in a fluidized bed. They then utilized trigonometric functions

to determine the 3D orientation of the cylinders. Inspired by these References [33,35,37-38], we established a new method to characterize the orientation of the cylinder during its suspension.
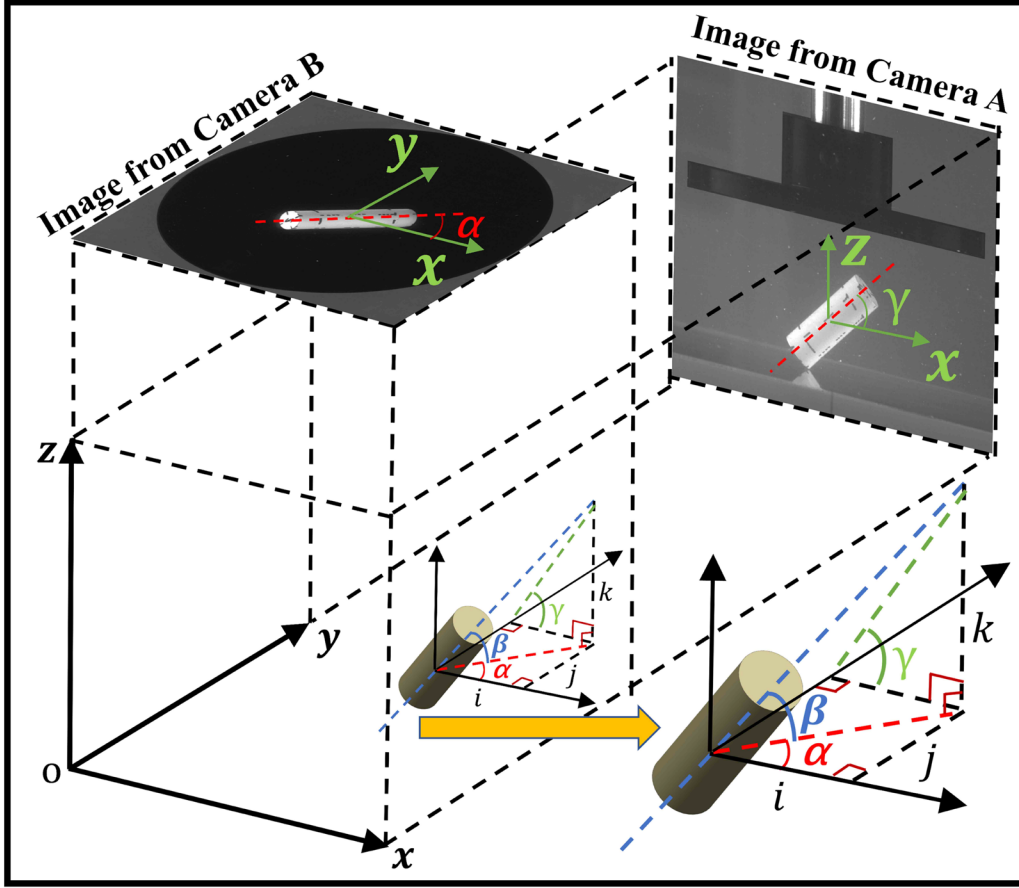

Fig. 3 - Azimuth angle α and elevation angle β of cylinder (the angle γ is an auxiliary angle). The i, j, k are the components of the cylinder's orientation unit vector in x, y, z coordinates.

Fig. 3 schematically shows how the orientation of a cylinder was determined. As the (i, j, k) are the three components of the unit vector representing the orientation of the cylinder, the angle α between the x axis and the projection of the cylinder in the x-y plane satisfies the following equation:

$$\tan \alpha = \frac{j}{i} \tag{1}$$

Similarly, the angle γ between the x axis and the projection of the cylinder in the x-z plane satisfies the following equation:

$$\tan \gamma = \frac{k}{i} \tag{2}$$

And the angle β between the cylinder's axis and the x-y plane satisfies the following equation:

$$\tan \beta = \frac{k}{\sqrt{i^2 + j^2}} \tag{3}$$

Substituting Eq. (1) and Eq. (2) into Eq. (3) yields:

$$\tan \beta = \frac{i \tan \gamma}{\sqrt{i^2 + i^2 \tan^2 \alpha}} \tag{4}$$

After simplifying Eq. (4), the angle β can be determined as follows:

$$\tan \beta = |\cos \alpha| \cdot \tan \gamma \tag{5}$$

As we measured the angles α and γ directly in the experiments, we then can calculate the angle β. The calculation of the elevation angle (beta) depends on the azimuth angle (alpha) and the auxiliary angle (gamma). The angles gamma and alpha are independent. Finally, we choose the azimuth angle α and the elevation angle β to represent the orientation of the cylinder. The angle α ranges from 0° to 360°, and the angle β from 0° to 90°.

3. Results and discussion

3.1. Critical lift-off impeller speed N_{LO}

We listed the results of lift-off experiments in the Appendix (Table S1). All particles are made of the same solid material and therefore all have the same density. We therefore expect the impeller speed to achieve lift-off to increase with increasing volume of the particle.
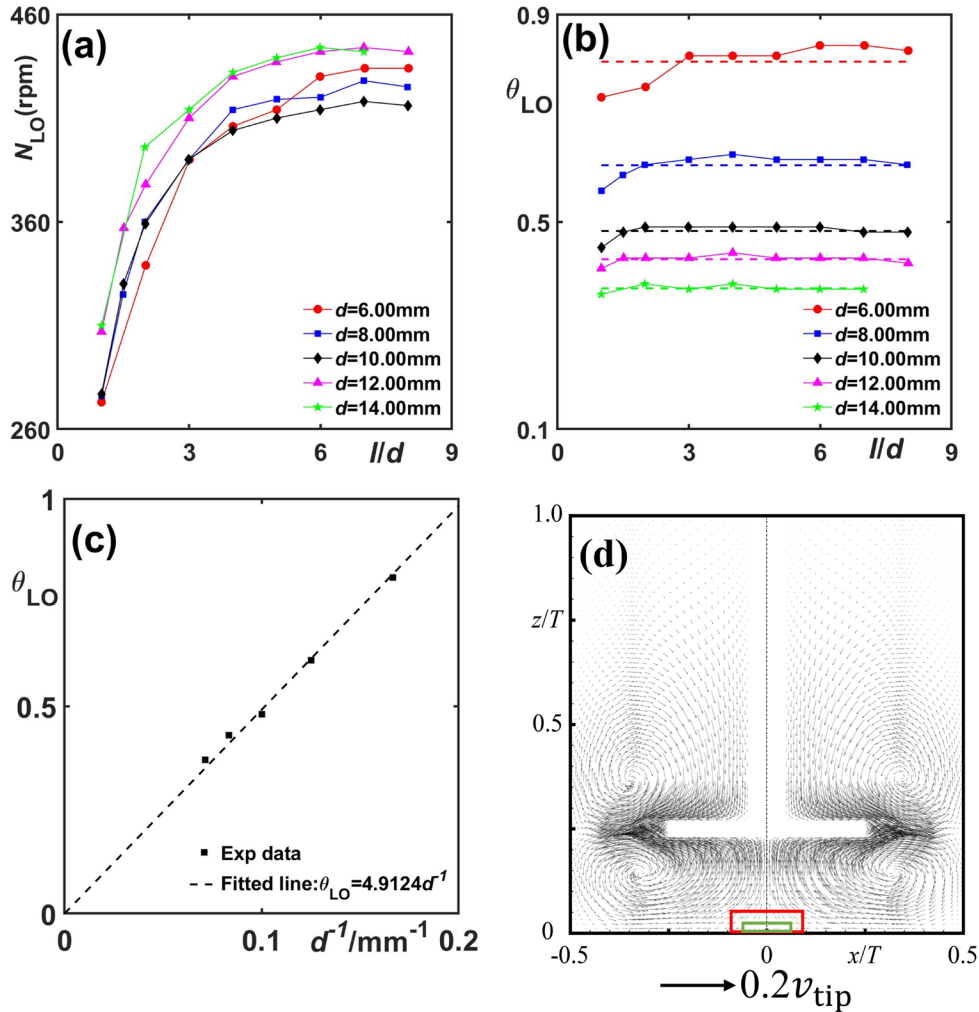
Fig. 4 - (a) Critical impeller speed to lift off the cylinder (N_{LO}) versus cylinder's aspect ratio, five diameters of cylinder as indicated. (b) Lift-off Shields number versus cylinder's aspect ratio l/d. The values of dashed horizontal lines are the average lift-off Shields number per diameter, which are used in panel (c) as well. (c) Average lift-off Shields number per diameter versus d^{-1}. (d) Impression of the simulated steady liquid flow (single phase) at $Re = 42.54$ in terms of velocity vector (vertical cross-section at $y = 0$). The green solid rectangle represents the cylinder with $d = 6.00$ mm and $l = 35.94$ mm. The red solid rectangle represents the cylinder with $d = 12.00$ mm and $l = 48.00$ mm. The N_{LO} for them both are 430 rpm.

Fig. 4 (a) shows the critical impeller speed N_{LO} to lift off the cylinder with five different diameters as a function of the cylinder's aspect ratio l/d. One trend that can be discerned in the Fig.4 (a) is an initial increase of N_{LO} with aspect ratio and then (beyond an l/d of approximately 5 to 6) N_{LO} levels off or even decreases. The latter implies that at that rotational speed of the disk the hydrodynamic force responsible for lifting off the particle is more or less proportional to the length of the cylinder. For l/d smaller than 4, it clearly is easier to suspend the shorter cylinder – likely due to its larger surface to volume ratio.

Fig. 4 (a) also shows – quite surprisingly – that except for the cylindrical particles with diameters of 12.00mm and 14.00mm, when $l/d>5.0$, the N_{LO} decreases with increasing diameter. This, in our opinion, demonstrates the influence of the way and extent to which the cylinders are exposed to the fluid flow. The same data as in Fig. 4 (a) have been rescaled in Fig. 4 (b): instead of the lift-off impeller speed, the vertical axis now shows the viscous Shields number θ. Clearly, θ is able to capture the effect of the aspect ratio: for a certain diameter of the cylinder, θ_{LO} is to a very good approximation independent of l/d. Given that the denominator of θ is the net weight of the cylinder, the numerator of θ (μNS) therefore is proportional to the hydrodynamic force lifting off the particle. The laminar flow conditions then dictate that that force is proportional to the dynamic viscosity μ and the impeller speed N. Given the results in Fig. 4 (b), the surface area S in the Shields number accounts well for the effect the aspect ratio l/d has on the suspension process. Fig. 4 (c) shows that θ_{LO} for the situations investigated here is to a good approximation inversely proportional to the cylinder diameter d. This dependency represents the effect of the exposure of the cylinder to the fluid flow generated by the rotating disk. Martino et al.' s research (Martino et al., 2009) shows that the initial motion of cylindrical particles is related to their area exposed to shear flow. It can be appreciated by looking at Fig. 4 (d) that shows an impression of the single-phase flow in the mixing tank at a representative Reynolds number of 42.54 (Mo et al.,

2015). The lattice–Boltzmann method was used to solve the single-phase flow field, and the numerical details could be referred to the work (Mo et al., 2015). It proves that the further the cylinder protrudes in this laminar flow, i.e. the larger its diameter, the stronger it feels the flow and thus the lower the value of θ required for its suspension.

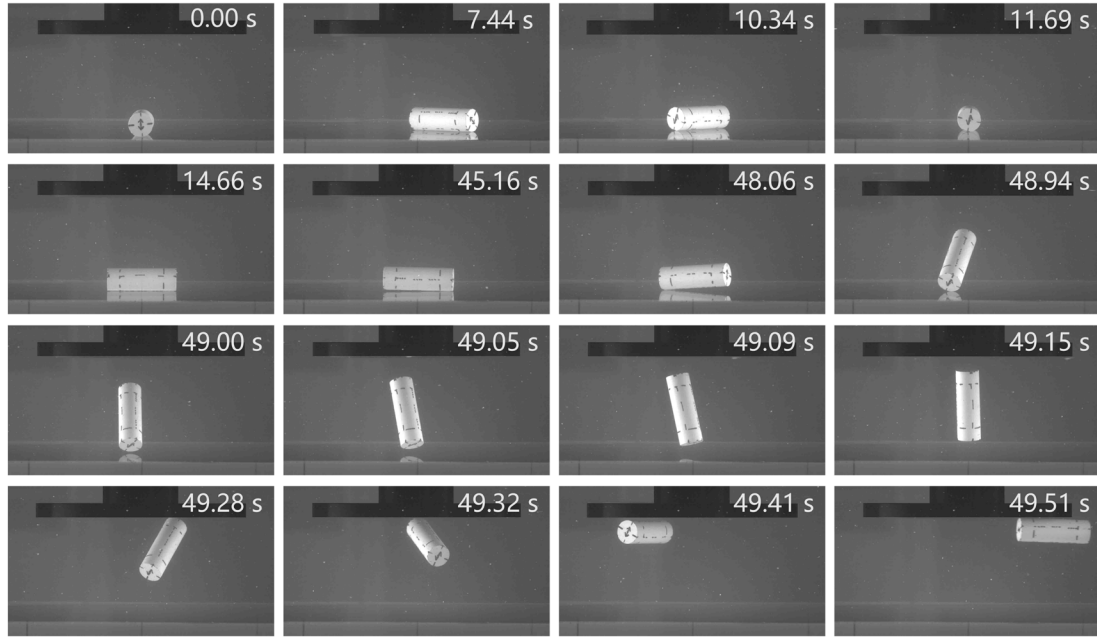### 3.2. Reproducibility of monitoring the lift-off & suspension process

Fig. 5 - The lift-off process for the cylinder with d = 12.00 mm and l/d = 3.00. The time at the moment of cylinder's position was given in each panel, and t = 0 was defined as the moment the impeller started.

The process of cylinder suspension is shown in Fig. 5. We divide the suspension process into three stages. During Stage 1, the cylinder moves over the tank bottom from the initial position to near the center of the tank bottom and then it moves and rotates over the bottom of the tank as a result of the flow generated by the spinning disk. Its main motion in this stage is spinning around a vertical axis along with translation over a path slightly away from the center of the bottom. During this stage, the cylinder will rotate progressively fast. It is interesting that the slight off-center location of the cylinder is different from that of the sphere, as the sphere rotates exactly in the center of the tank bottom in Stage 1 (Wang et al., 2019). In Stage 2, one end of the cylinder rises first and its elevation increases gradually. After the whole cylinder has detached from the bottom wall, it translates vertically toward the disk thereby continually changing its orientation. Upon approaching the lower surface of the disk, it gets oriented horizontally. In Stage 3, the cylinder

swirls underneath the disk and then gets ejected into the bulk of the tank. The first stage takes most time (up to 60 s); the other two stages take 1 to 2 s (see Fig. 5).

The phenomena shown in Fig. 5 are also valid for the cylinder with $l/d = 1.00$ in its initial suspension. But during resuspension, one of the end surfaces might land on the bottom, and then the cylinder could not be lifted off anymore. That is, the flat surface contact is more difficult to be broken.

In this section we are primarily concerned with the reproducibility of the suspension process. This is mainly because in our largely axisymmetric flow geometry we observe departures of the cylinder from the centerline during Stage 1 of suspension as well as lifting off of the cylinder from one side first during Stage 2. This might have to do with inherent instabilities and/or slight (random) imperfections in the mixing tank or cylinder geometry.

In order to reduce error in image processing, in this section we only consider the cylinder with $d = 12.00$ mm and $l/d = 3.00$ so that we can increase the number of pixels occupied by the image of the cylinder. In addition, we want the cylinder to be able to assume a vertical orientation while rising to the spinning disk so that its length should be smaller than the distance between the lower disk surface and the bottom of the tank.
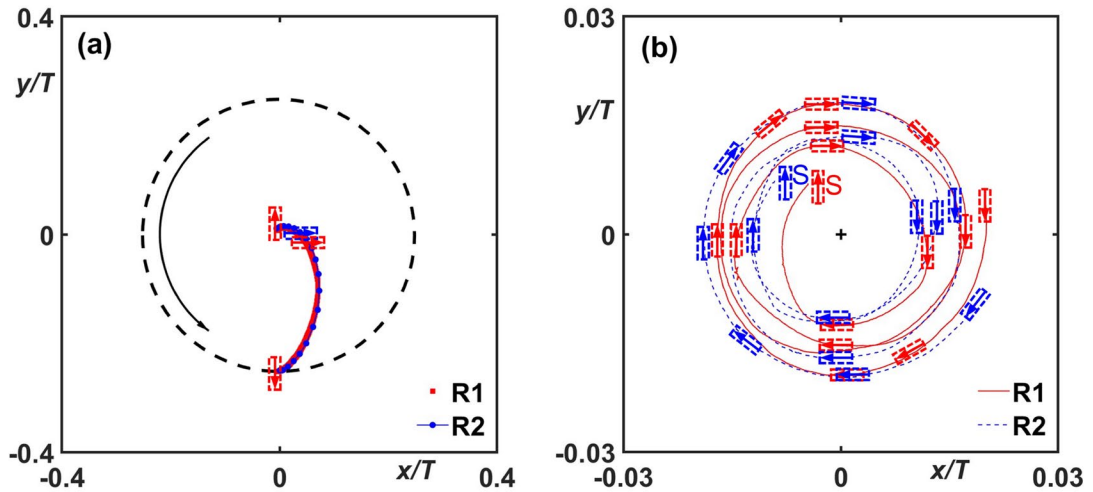

Fig. 6 - Stage 1: Cylinder's motion over the bottom for the cylinder with $d = 12.00$ mm and $l/d = 3.00$. In this view the disk rotates in the counterclockwise direction. (a) The cylinder moves from its initial position to near the center of the tank bottom where α of the cylinder is 90°; (b) the cylinder moves in a quasi-circular motion around the center of the tank bottom as marked with a black cross, and the starting points marked with "S" in this panel coincide with the ending points in the left panel. "R1" and "R2" are two realizations at the same experimental conditions.

For two realizations of the experiment with a cylinder with d = 12.00 mm and l/d = 3.00, the results of the quantitative visualizations are shown in Figs. 6-8. Overall, the experiment shows good reproducibility in all three stages. As shown in Fig. 6 (a), the cylinders move from the initial position to the near center of the tank bottom, and there is almost no difference between the two realizations. We define the azimuth angle α of the cylinder in the initial position as 270°, and α changes from 270° to 360° (or 0°) and to 90° in this panel. In Fig. 6 (b), we can see that the cylinder's centroid location gradually shifts away slightly from the bottom center. Though the trajectories for the two realizations are not the same, they show the same pattern with comparable radial location as a function of time (note that the radial centroid positions are of the order of 0.01T which only is a few millimeter). During this stage, the flow makes the cylinder roll and/or slide over the bottom with the cylinder having a line contact with the bottom wall. We also added dotted rectangles in Fig. 6 as well as Figs. 8 and 12 (they are approximately 2.5% of the actual size of the cylinders) to display the azimuth angle α of the cylinder at different locations. At the beginning, its orientation is uncorrelated with its trajectory. When the cylinder has moved further away from the center, it tends to orient tangentially until one end rises and the cylinder lifts off. In addition, we find that the trajectory reproducibility of the last loop before the cylinder is lifted off is better than the previous loops for the two realizations. That is, the effect of instability or random parameters such as roughness on the offset distance diminishes gradually near the lift-off moment. We will focus on parameters influencing the offset distance before lifting off in section 3.3.
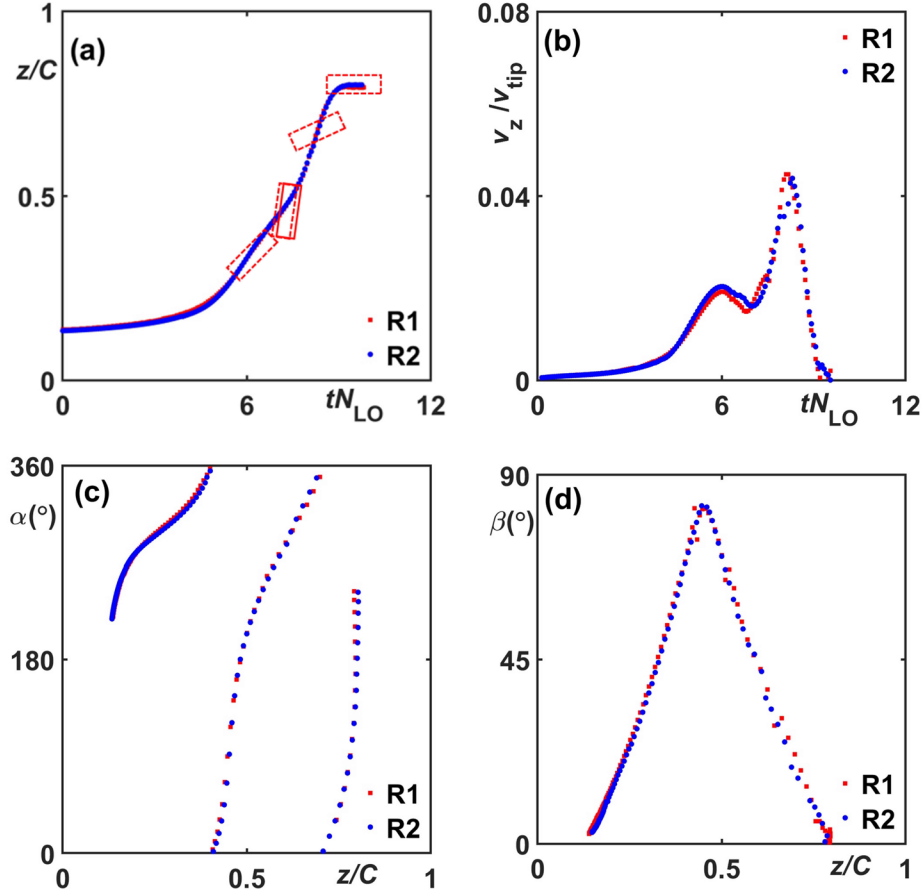
Fig. 7 - Stage 2: Cylinder's rising motion to the disk for the cylinder with $d = 12.00$ mm and $l/d = 3.00$. (a) The cylinder's vertical location as a function of time; (b) the cylinder's vertical velocity as a function of time; (c) the azimuth angle α as a function of vertical height; (d) the elevation angle β as a function of vertical height. In panels (a) and (b), $t = 0$ is defined as the moment when the cylinder's centroid height $z = (0.5+0.1)d$. "R1" and "R2" are two realizations at the same experimental conditions.

Fig. 7 shows the process of the cylinder rising from the bottom towards the spinning disk for two realizations of the experiment (R1 and R2). The way the cylinder orientation changes first from horizontal to vertical and then back to horizontal agrees well between R1 and R2, as shown in Fig.7 (a), and the dotted rectangles (they are approximately 5.0% of the actual size of the cylinders) are added to display the elevation angle β of the cylinder at different times, the solid line rectangle is added to display the max elevation angle β of the cylinder at $z/C \approx 0.45$. This effect has been further detailed in Fig. 7 (d) that shows the elevation angle β as a function of the vertical cylinder location. It is striking to see a very sharp peak in β at $z/C \approx 0.45$. The vertical velocity of the cylinder in Fig. 7 (b) was calculated by using numerical differentiation:

$$v_z(i) = \frac{z(i-2) - 8z(i-1) + 8z(i+1) - z(i+2)}{12\Delta t} \qquad (6)$$

with $z(i)$ vertical coordinate at moment i, and $\Delta t = 0.01s$ the time interval between two camera frames. In addition, the azimuth angle α shows very reproducible behavior as well, see Fig. 7(c).
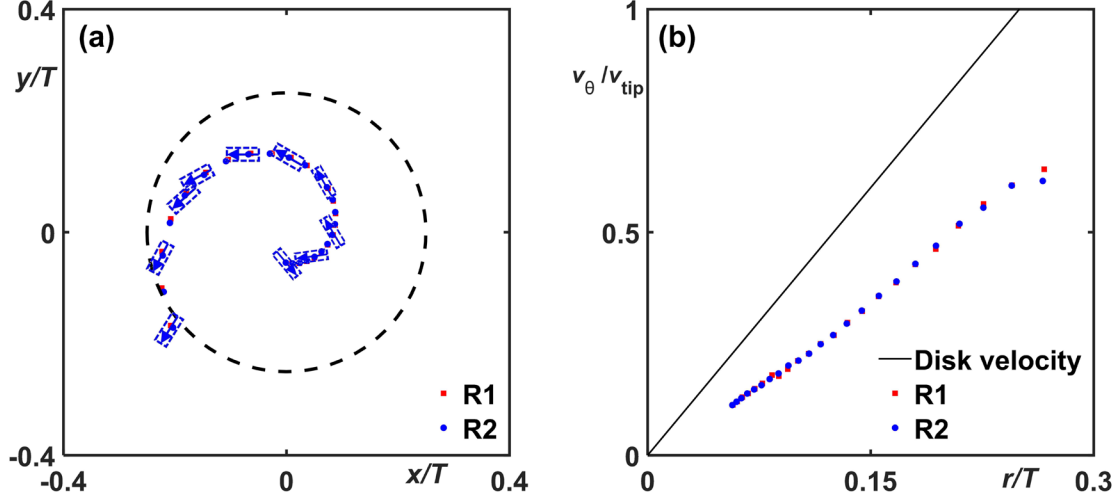

Fig 8 - Stage 3: (a) Cylinder's motion underneath the disk for the cylinder with $d = 12.00$ mm and $l/d = 3.00$. (b) The tangential velocity of the cylinder as a function of its radial location. The straight line represents the solid body rotation of the disk. Comparison between two realizations R1 and R2 of the experiment.

The cylinder's swirling motion underneath the spinning disk is illustrated in Fig. 8. At this Stage 3 of the suspension process, there is a narrow gap between the cylinder and the disk (see the panel at $t = 49.41$ s Fig. 5). When the elevation angle β is less than 10°, we suppose the cylinder is approximately parallel to the x-y plane so that only the azimuth angle α is analyzed. The strong rotational motion of the cylinder and associated centrifugal force make that it aligns with the horizontal trajectory until it reaches the edge of the disk where it is caught by the bulk flow in the mixing tank which slows down the far end of the cylinder. As before, we see good reproducibility between realizations R1 and R2.

During Stage 1 of the suspension of the cylinder, the translation over the bottom wall is a combination of rolling and sliding. To quantitatively describe the rolling and sliding, we drew two orthogonal rectangles on the surface of the cylinder, two circles with different dashed lines on the cylindrical surface, and two types of arrows with the same direction on each end surface, as shown in Fig. 9. In the last panel of Fig. 9, the cylinder's centroid height is lifted to $z = (0.5+0.1)d$ at 47.02s. We define both the self-rolling angle ω and azimuth sliding angle α as 0° at 35.42 s, and the two angles at each moment were calculated by utilizing the side view and bottom view of the

cylinder. The right-hand rule can be used to determine the rolling direction of the cylinder. With the thumb pointing to the end surface of the cylinder with the complete arrows (see the arrows at 37.82 s) along the cylinder's axis, the cylinder rolls in the direction of the fingers closing on the palm. It is interesting to note that the self-rolling, as well as the azimuth sliding, are more and more obvious when the cylinder approaches being lifted off, if we compare the cylinder movements in the middle row and those in the bottom row.
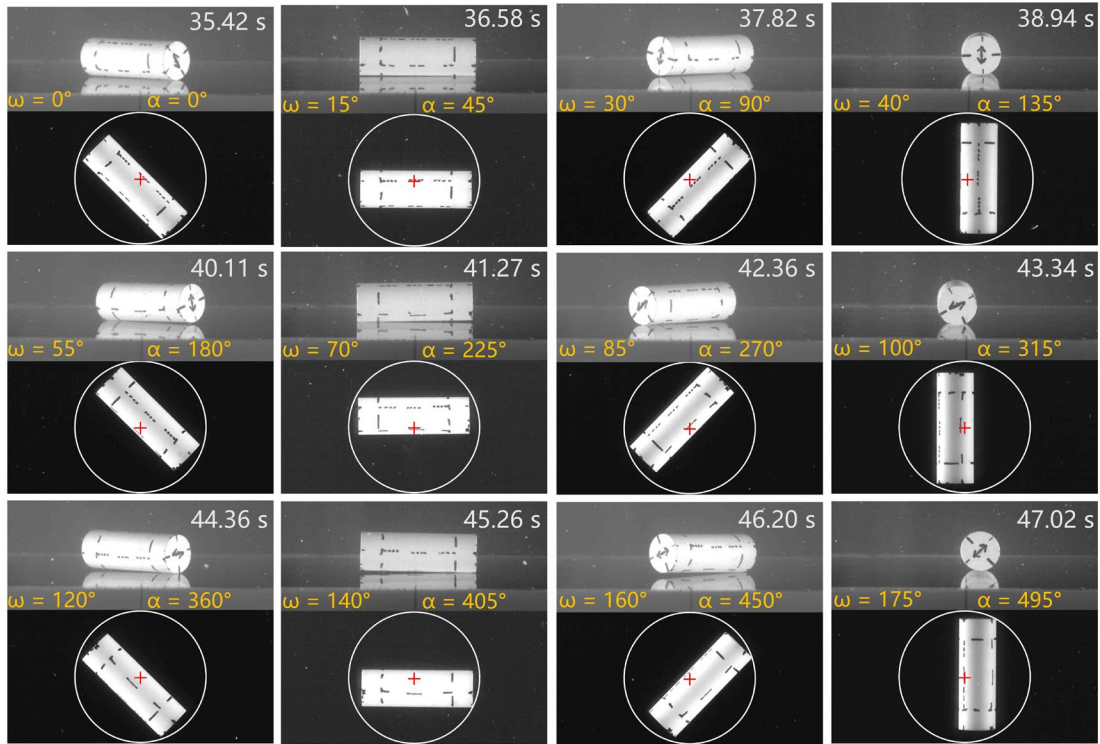

Fig. 9 - Cylinder rolling and sliding over the bottom during lift-off process. Upper part of each panel is the side view of the cylinder, and lower part of each panel is the bottom view. The radius of the white circle is 22 mm and its center is the bottom center of the tank as marked with a red cross. In the bottom view, the disk rotates in the counterclockwise direction. The angle ω is a self-rolling angle around the cylinder axis.

3.3 The effect of aspect ratio on the lift-off & suspension process

At each stage, the visualization results for six cylinders of diameter $d = 12.00$ mm with six different aspect ratios are compared, illustrating systematically the influence of aspect ratio ranging from 1 to 6 on the suspension process. When $l/d \geq 5.0$, the length of the cylinder is larger than the off-bottom clearance of the disk so that it cannot get upright ($\beta = 90$) in Stage 2. Fig. 10 (a) shows trajectories of the centroid of the cylinders moving over the bottom (Stage 1) until the moment they get lifted off. It is found that aspect ratio has negligible effect on the trajectories. But if we zoom in the trajectories near the bottom center, we can observe that the higher the aspect

ratio, the farther away from the center lift-off occurs, see Fig. 10 (b). This likely is because the hydrodynamic forces and the asymmetry of their distribution over the length of the cylinder get stronger with greater distance from the center of the bottom of the mixing tank.
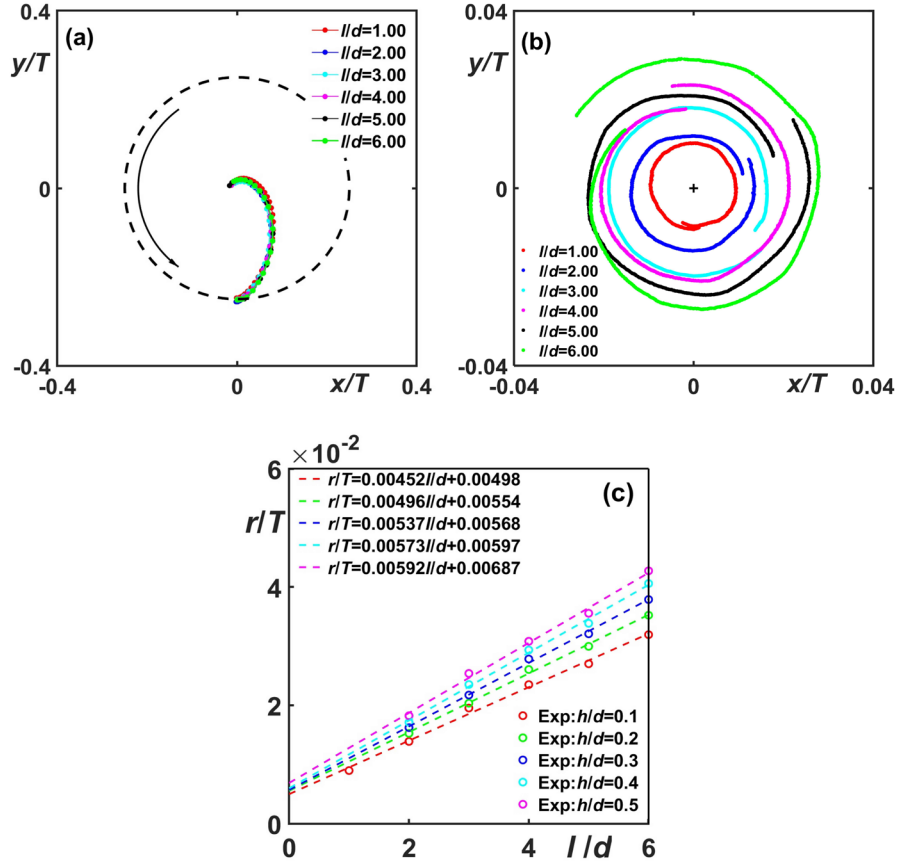

Fig. 10 - Effect of aspect ratio on the cylinder's rotating motion over the bottom. (a) The cylinder moves from the initial position to near the center of the tank bottom ($\alpha = 90°$); (b) the last loop of the cylinder moving around the tank bottom center as marked with a black cross; (c) radial location of the cylinder as a function of aspect ratio l/d at five lift-off heights $h = z$-0.5d. Cylinder diameter is $d = 12.00$ mm.

We calculated the ultimate offset distance r which is the radial distance between the cylinder's centroid and the center of tank bottom at the lift-off moment at which the cylinder center was lifted to $z = (0.5+0.1)d$. We also calculated r for the cylinder being lifted to various heights and ensured that one end of the cylinder is still in contact with the tank bottom. Fig. 10 (c) shows the offset distance r, which is the average value of two realizations, as a function of the aspect ratio. Good linear correlations are obtained for each h/d with coefficient of determination R^2 larger than 0.99. Every linear relationship is observed with a non-zero intercept meaning that also very short cylinders would require some deviation from the tank bottom before they can be lifted off. We

also find that the offset distance r is positively correlated with h for the same cylinder, which means that the cylindrical particles do not rise along a vertical line toward the disk compared with spherical particles (Mo et al., 2015).

The vertical motion (Stage 2) of the cylinders is analyzed in Fig. 11. As the error of the elevation angle β for the cylinder with aspect ratio of 1.00 is too large, we remove the panel on its elevation angle versus vertical position. The ultimate vertical height of cylinder's centroid decreases with increasing aspect ratio as shown in Fig. 11 (a). The shortest cylinder with the aspect ratio of 1.00 could be lifted to the height $z = 0.813C$. If a horizontally oriented cylinder were to touch the disk, its centroid would be at $z = 45.315$ mm $= 0.824C$. We thus see that there remains a gap between the spinning disk and the suspended cylinder with the gap width increasing with aspect ratio.

Fig. 11 (b) shows that the vertical velocity profiles of all cylinders have two peaks. We thus found that all six cylinders briefly decelerate on their way up. For the cylinders with $3.00 \leqslant l/d \leqslant 6.00$, the deceleration happens at the height of $z \approx 0.45C$. At this vertical level, the velocity field underneath the disk in the vertical center plane changes from converging (radially inward) to diverging (radially outward) as shown in Fig. 4(d). For the cylinder with $4.00 \leqslant l/d \leqslant 6.00$, its highest end point is so close to the disk at this moment that it only can rise very slowly, which corresponds with and almost zero vertical velocity (i.e. a plateau in the height versus time curve). Especially, for the cylinders with $5.00 \leqslant l/d \leqslant 6.00$, when one end of the cylinder is in contact with the bottom surface of the disk, the other end of the cylinder is still in contact with the tank bottom. As a result of its decrease in β, the closest distance between cylinder and disk increases and the cylinder rises faster again. Similar effects are observed for the shorter cylinder with $l/d = 3.00$. For the cylinder with $l/d = 1.00$ and 2.00, their decelerations happen at the height of $z \approx 0.785C$ and $0.66C$ respectively. As for the cylinder with $4.00 \leqslant l/d \leqslant 6.00$, it decelerates because of inadequate space between its height point and the lower rotating disk surface.

For cylinders with $l/d = 1.00$, the maximum lift-off height $z = 0.813C$ could be achieved in two situations: one is that the axis of the cylinder is almost perpendicular to the disk, and another is that the axis is almost parallel to the disk. Furthermore, the two situations appear alternatively while the cylinder is approaching the disk, which cause the fluctuations of vertical locations in Fig. 11 (a) and of vertical velocity in Fig. 11 (b).
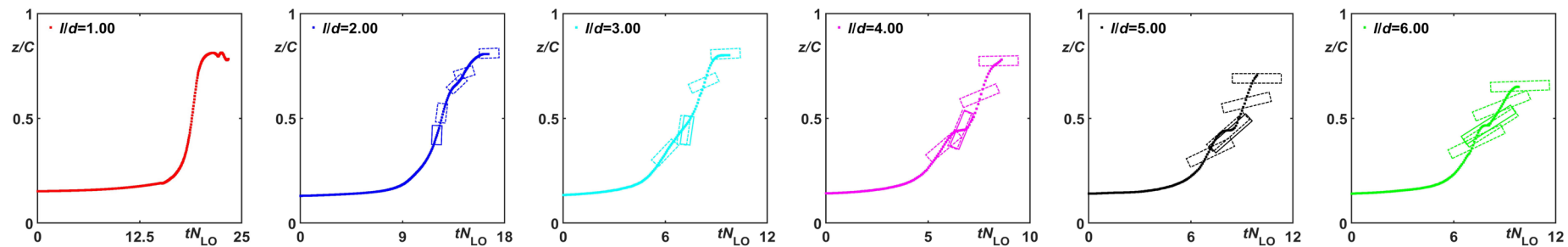
(a)
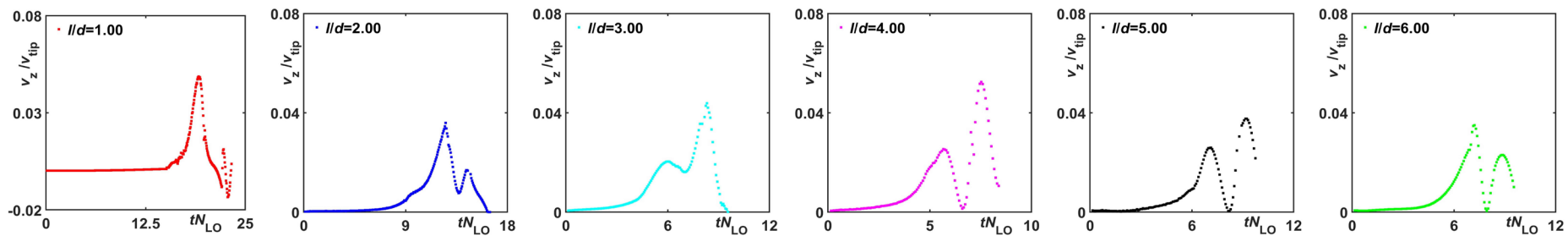
(b)
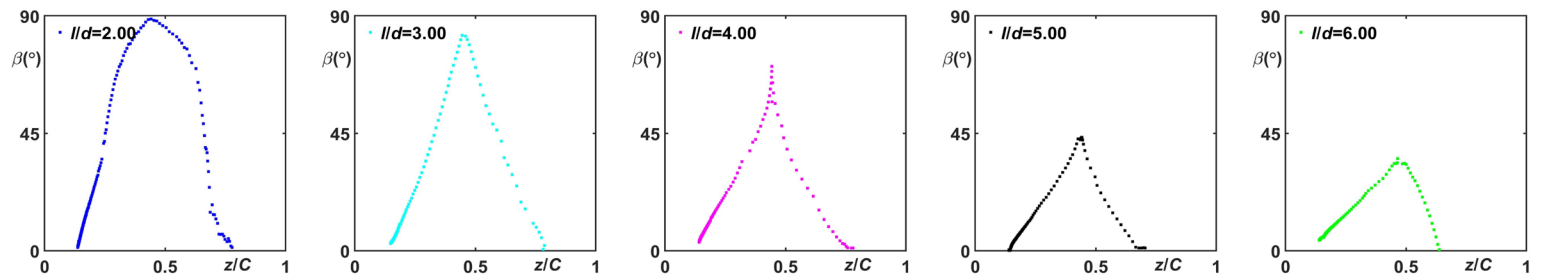
(c)

Fig. 11 - Effect of aspect ratio on cylinder's rising motion to the rotating disk. (a) The cylinder's vertical location as a function of time; (b) the cylinder's vertical velocity as a function of time; (c) the elevation angle β as a function of vertical height. Cylinder diameter $d = 12.00$ mm; aspect ratios l/d as indicated.

The relationship between the particle elevation angle β and the vertical position is shown in Fig. 11 (c), it is noted that the angle β of the five cylinders with $2.00 \leqslant l/d \leqslant 6.00$ reaches its peak value when the height of the cylinder's centroid is $z \approx 0.45C$. As previously described, this is the moment when they start turning from vertical to horizontal. In addition, the maximum value of β decreases with increasing aspect ratio as a result of the limited space between the tank bottom and the disk.

To eliminate the influence of parallax while reconstructing the 3D coordinates of the cylinders, a 3D reconstruction principle (Cui et al., 2014; Lei et al., 2014; Zhang, 2000) was used and then the 3D trajectories of the cylinders with $1.00 \leqslant l/d \leqslant 6.00$ were obtained, see Fig. 12 (a). The starting point corresponds to the moment when the particle is lifted to $z = (0.5+0.1)d$ and the end point the moment with radial distance of the cylinder $r = 0.5D$.
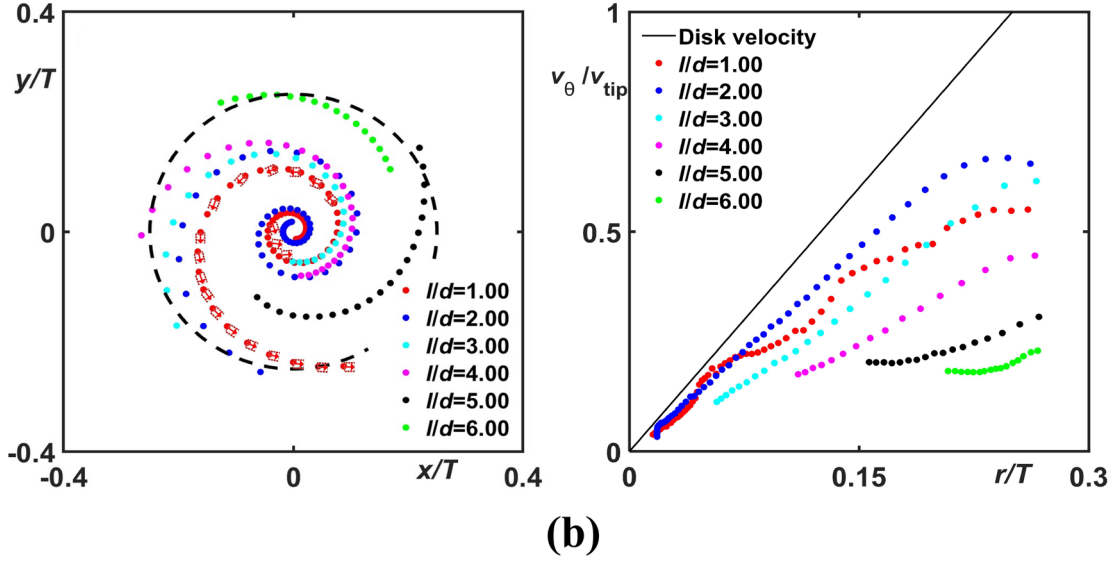

(a)
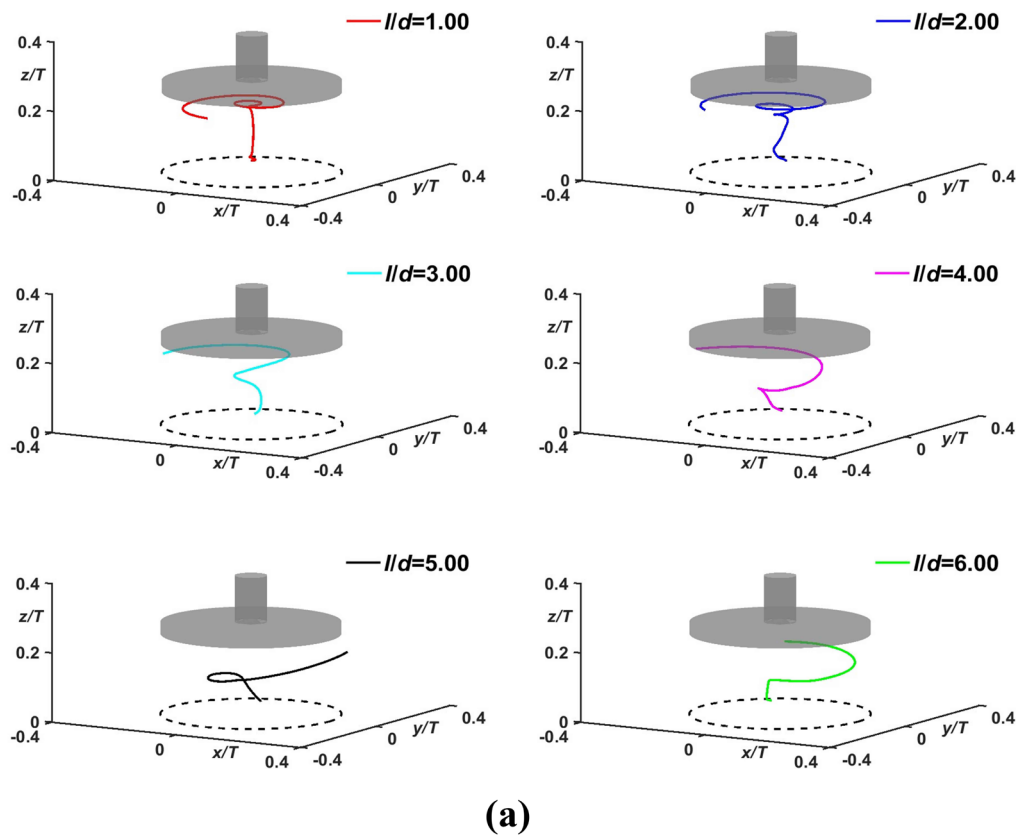
Fig.12 - (a) Three-dimensional trajectories of the cylinders. (b) Left panel: effect of aspect ratio on cylinder's motion underneath the disk. Right panel: tangential velocity of the cylinder as a function of its radial location. Cylinder diameter d = 12.00 mm; aspect ratios l/d as indicated.

Fig. 12 (b) shows the comparison for the cylinders' swirling motion underneath the disk. The longest cylinder follows a shorter and more outside swirling path than the other five cylinders because the initial position for the longer cylinder is farther from the center than the shorter cylinder. As shown in the right panel of Fig. 12 (b), except for the cylinder with l/d = 1.00, the tangential velocity of the cylinders near the disk bottom decreases with increasing l/d. The particularity of the cylinder with l/d = 1.00 is that the strong rotational motion of the cylinder and associated centrifugal force make that it rolls rather than aligns with the horizontal trajectory until it reaches the edge of the disk. This is why its velocity fluctuates as a function of the radial position. The orientation is very close to the tangential direction of the trajectory for the cylinders with l/d ranging from 1 to 6.

4. Conclusions

In this article, we investigated experimentally a single cylinder suspension in a laminar flow driven by a spinning disk. We employed various PTFE cylinders with different diameters and aspect ratios and measured the critical rotational speed of the disk to achieve lift-off N_{LO}. The cylinder's rising translational and rotational motion were captured by two cameras operated at 100 frames per second. We defined two angles to describe the orientation of the cylinder and used quantitative image analysis to obtain the detailed information on the motion of the cylinder.

The uncertainty of the measurement of the critical impeller speed N_{LO} is less than 1%. The

experiments show that the parameters controlling the suspension process are the viscous Shields number θ as well as the cylinder's diameter which is the distance the cylinder protrudes into the laminar liquid flow above the tank bottom. Regarding the Shields number, involving in it the surface area of the cylinder is a good way to account for the cylinder's aspect ratio.

The cylinder's suspension process has been divided into three stages: 1) moving from the initial position to near bottom center and then moving over the tank bottom to an off-center location, 2) rising toward the disk, and 3) swirling underneath the disk. All three stages were analyzed in terms of the centroid location, the azimuth angle α and elevation angle β. The trajectories and orientations of the cylinder at three stages are highly reproducible in the experiments although the time required for suspension presents some random characteristics. The cylinder's surface roughness may be the main reason for this randomness. We quantitatively identified the sliding and rolling angles of cylinders before lift-off and found that the off-center sliding and self-rolling are more and more evident for the cylinders being lifted off.

We investigated the influence of aspect ratio on the cylinders' motion. The cylinder's deviation distance from the center of the bottom wall at lift off is almost linearly related to its aspect ratio. The cylinder's upward motion is somewhat restricted by the limited space underneath the disk. This has the strongest impact on the longer cylinders. For a cylinder with aspect ratio of 1.00, we found a special phenomenon that two different situations appear alternatively while the cylinder is approaching the disk.

The information collected in this paper on a relatively simple system (one cylinder, laminar flow) is accurate validation material for critical assessment of computational methods to be used for the study of agitated suspension processes involving non-spherical solid particles under more challenging circumstances such as dense multi-particle systems mobilized by turbulent flow.

Acknowledgments

Nomenclature

C	Off-bottom clearance of the disk [m]
d	Cylinder diameter [m]
D	Disk diameter [m]
g	Gravitational acceleration [m/s^2]
h	Lift-off height of cylinder [m]
H	Liquid height inside the tank [m]
i, j, k	The components of the cylinder's orientation unit vector [−]
l	Cylinder length [m]
N	Impeller speed [revolution/s]
N_{LO}	Critical lift-off impeller speed [revolution/s]
r	Radial location [m]
Re	Reynolds number based on impeller speed, $Re = ND^2/v$ [−]
Re_{LO}	Reynolds number based on critical lift-off impeller speed, $Re = N_{LO}\,D^2/v$ [−]
S	Surface area of the cylinder [m^2]
t	Time [s]
T	Side length of the tank [m]
T_m	Average temperature inside the tank [°C]
v_θ	Tangential velocity of cylinder [m/s]
v_{tip}	Tip speed of the disk [m/s]
v_z	Lift-off velocity of cylinder [m/s]
V	Volume of the cylinder [m^3]
x, y, z	Cartesian coordinates [m]

Greek letters

α	Azimuth angle [°]
β	Elevation angle [°]
γ	Auxiliary angle of cylinder [°]
θ	Shields number, $\theta = \mu NS/g(\rho_P\text{-}\rho)V$ [−]
θ_{LO}	Shields number based on critical lift-off impeller speed, $\theta = \mu\,N_{LO}\,S/g(\rho_P\text{-}\rho)V$ [−]
μ	Dynamic viscosity of the silicone oil [Pa·s]
v	Kinematic viscosity of the silicone oil [m^2/s]

ρ Density of the silicone oil [kg/m^3]

ρ_{p} Cylinder density [kg/m^3]

ω Self-rotation angle of cylinder [°]

References

Baldi, G., Conti, R., Alaria, E., 1978. Complete suspension of particles in mechanically agitated vessels. Chemical Engineering Science 33, 21-25. http://dx.doi.org/10.1016/0009-2509(78)85063-5

Chen, X., Zhong, W., Heindel, T.J., 2019. Orientation of cylindrical particles in a fluidized bed based on stereo X-ray particle tracking velocimetry (XPTV). Chemical Engineering Science 203, 104-112. http://dx.doi.org/10.1016/j.ces.2019.03.067

Chhabra, R., Agarwal, L., Sinha, N.K., 1999. Drag on non-spherical particles: an evaluation of available methods. Powder Technology 101, 288-295. http://dx.doi.org/10.1016/S0032-5910(98)00178-8

Cui, Y., Zhou, F., Wang, Y., Liu, L., Gao, H., 2014. Precise calibration of binocular vision system used for vision measurement. Opt Express 22, 9134-9149. http://dx.doi.org/10.1364/OE.22.009134

Derksen, J.J., 2019. Liquid fluidization with cylindrical particles: Highly resolved simulations. AIChE Journal 65. http://dx.doi.org/10.1002/aic.16594

Derksen, J.J., 2020. Agitating cylindrical particles in laminar liquid flow. Chemical Engineering Research and Design 154, 11-20. http://dx.doi.org/10.1016/j.cherd.2019.12.002

Fan, L., Mao, Z.-S., Yang, C., 2004. Experiment on Settling of Slender Particles with Large Aspect Ratio and Correlation of the Drag Coefficient. Industrial & Engineering Chemistry Research 43, 7664-7670. http://dx.doi.org/10.1021/ie049479k

Fan, L., Xu, N., 2017a. Experimental investigation of fibre particles in a turbulent stirred tank with DPIV. Powder Technology 316, 329-337. http://dx.doi.org/10.1016/j.powtec.2016.10.065

Fan, L., Xu, N., 2017b. Study on laminar flow containing fibre particles in a stirred tank using DPIV. Powder Technology 320, 420-427. http://dx.doi.org/10.1016/j.powtec.2017.07.079

Haider, A., Levenspiel, O., 1989. Drag coefficient and terminal velocity of spherical and nonspherical particles. Powder Technology 58, 63-70. http://dx.doi.org/10.1016/0032-5910(89)80008-7

Haralick, R.M., Shapiro, L.G., 1992. Computer and Robot Vision, in: Computer and Information Science.

Jafari, R., Chaouki, J., Tanguy, P.A., 2012. A Comprehensive Review of Just Suspended Speed in Liquid-Solid and Gas-Liquid-Solid Stirred Tank Reactors. International Journal of Chemical Reactor Engineering 10. http://dx.doi.org/10.1515/1542-6580.2808

Jianzhong, L., Xing, S., Zhenjiang, Y., 2003. Effects of the aspect ratio on the sedimentation of a fiber in Newtonian fluids. Journal of Aerosol Science 34, 909-921. http://dx.doi.org/10.1016/s0021-8502(03)00039-9

Krueger, B., Wirtz, S., Scherer, V., 2015. Measurement of drag coefficients of non-spherical particles with a camera-based method. Powder Technology 278, 157-170. http://dx.doi.org/10.1016/j.powtec.2015.03.024

Lamberto, D.J., Alvarez, M.M., Muzzio, F.J., 1999. Experimental and computational investigation of the laminar flow structure in a stirred tank. Chemical Engineering Science 54, 919-942. http://dx.doi.org/10.1016/S0009-2509(98)00275-9

Lau, R., Hassan, M.S., Wong, W., Chen, T., 2010. Revisit of the Wall Effect on the Settling of Cylindrical Particles in the Inertial Regime. Industrial & Engineering Chemistry Research 49, 8870-8876. http://dx.doi.org/10.1021/ie1012807

Lei, M., Chen, M., Li, H., 2014. Goal's three-dimensional trajectory reconstruction based on the adaptive multiple target surface iteration method. Computer Modelling & New Technologies 18, 19-25.

Liu, Y.J., Joseph, D.D., 1993. Sedimentation of particles in polymer solutions. Journal of Fluid Mechanics 255, 565-595. http://dx.doi.org/10.1017/S0022112093002599

Martino, R., Paterson, A., Piva, M., 2009. Onset of motion of a partly hidden cylinder in a laminar shear flow. Phys Rev E Stat Nonlin Soft Matter Phys 79, 036315. http://dx.doi.org/10.1103/PhysRevE.79.036315

Mo, J., Gao, Z., Bao, Y., Li, Z., Derksen, J.J., 2015. Suspending a solid sphere in laminar inertial liquid flow-experiments and simulations. AIChE Journal 61, 1455-1469. http://dx.doi.org/10.1002/aic.14756

N. Sharma, R., A. Shaikh, A., 2003. Solids suspension in stirred tanks with pitched blade turbines. Chemical Engineering Science 58, 2123-2140. http://dx.doi.org/10.1016/s0009-2509(03)00023-x

Pang, S., 2019. Advances in thermochemical conversion of woody biomass to energy, fuels and chemicals. Biotechnol Adv 37, 589-597. http://dx.doi.org/10.1016/j.biotechadv.2018.11.004

Qi, D., 2001. Simulations of fluidization of cylindrical multiparticles in a three-dimensional space. International Journal of Multiphase Flow 27, 107-118. http://dx.doi.org/10.1016/S0301-9322(00)00008-2

Qi, G., Nathan, G.J., Kelso, R.M., 2014. The influence of aspect ratio on distributions of settling velocities and orientations of long fibres. Powder Technology 257, 192-197. http://dx.doi.org/10.1016/j.powtec.2014.02.050

Qi, G.Q., Nathan, G.J., Kelso, R.M., 2012. PTV measurement of drag coefficient of fibrous particles with large aspect ratio. Powder Technology 229, 261-269. http://dx.doi.org/10.1016/j.powtec.2012.06.049

Salmela, J., Martinez, D.M., Kataja, M., 2007. Settling of dilute and semidilute fiber suspensions at finiteRe. AIChE Journal 53, 1916-1923. http://dx.doi.org/10.1002/aic.11245

Takahashi, K., Sugo, Y., Takahata, Y., Sekine, H., Nakamura, M., 2012. Laminar mixing in stirred tank agitated by an impeller inclined. International Journal of Chemical Engineering 2012. http://dx.doi.org/doi.org/10.1155/2012/858329

Tran-Cong, S., Gay, M., Michaelides, E.E., 2004. Drag coefficients of irregularly shaped particles. Powder Technology 139, 21-32. http://dx.doi.org/10.1016/j.powtec.2003.10.002

Turney, M.A., Cheung, M.K., Powell, R.L., McCarthy, M.J., 1995. Hindered settling of rod-like particles measured with magnetic resonance imaging. AIChE Journal 41, 251-257. http://dx.doi.org/10.1002/aic.690410207

Unnikrishnan, A., Chhabra, R., 1991. An experimental study of motion of cylinders in Newtonian fluids: wall effects and drag coefficient. The Canadian Journal of Chemical Engineering 69, 729-735. http://dx.doi.org/10.1002/cjce.5450690315

van den Boomgaard, R., van Balen, R., 1992. Methods for fast morphological image transforms using bitmapped binary images. CVGIP: Graphical Models and Image Processing 54, 252-258. http://dx.doi.org/10.1016/1049-9652(92)90055-3

Wang, C., Wang, H., Zhang, K., Li, Z., Gao, Z., Derksen, J.J., 2019. Lifting off a solid sphere from a

flat bottom by laminar fluid flow. AIChE Journal 66. http://dx.doi.org/10.1002/aic.16886

Wang, C., Zhang, L., Li, Z., Gao, Z., Derksen, J.J., 2018. Multi-particle suspension in a laminar flow agitated by a Rushton turbine. Chemical Engineering Research and Design 132, 831-842. http://dx.doi.org/10.1016/j.cherd.2018.02.035

Zalc, J., Alvarez, M., Muzzio, F., Arik, B., 2001. Extensive validation of computed laminar flow in a stirred tank with three Rushton turbines. AIChE Journal 47, 2144-2154. http://dx.doi.org/10.1002/aic.690471003

Zhang, L.J., Yu, W.D., 2017. Orientation image analysis of electrospun submicro-fibers based on Hough transform and Regionprops function. TEXTILE RESEARCH JOURNAL 87, 2263-2274. http://dx.doi.org/10.1177/0040517516669070

Zhang, Z., 2000. A flexible new technique for camera calibration. IEEE Transactions on pattern analysis and machine intelligence 22, 1330-1334. http://dx.doi.org/10.1109/34.888718

Zheng, C., Guo, J., Wang, C., Chen, Y., Zheng, H., Yan, Z., Chen, Q., 2019. Experimental study and simulation of a three-phase flow stirred bioreactor. Chinese Journal of Chemical Engineering 27, 649-659. http://dx.doi.org/10.1016/j.cjche.2018.06.010

Zwietering, T.N., 1958. Suspending of solid particles in liquid by agitators. Chemical Engineering Science 8, 244-253. http://dx.doi.org/10.1016/0009-2509(58)85031-9

Appendix
Table S1

Table S1. Lift-off impeller speed N_{LO} for various cylinders and derived quantities

Case	d(mm)	l(mm)	$l/d(-)$	$N_{LO}(rpm)$	$R_{eLO}(-)$	S(mm²)	$\theta_{LO}(-)$
E1	6.00	6.00	1.00	273	27.01	169.65	0.74
E2		12.03	2.01	339	33.54	283.31	0.76
E3		18.05	3.01	390	38.59	396.78	0.82
E4		24.02	4.00	406	40.17	509.32	0.82
E5		30.01	5.00	414	40.96	622.22	0.82
E6		35.94	5.99	430	42.54	734.00	0.84
E7		42.05	7.01	434	42.94	849.17	0.84
E8		48.06	8.01	434	42.94	962.46	0.83
E9	8.00	7.99	1.00	276	27.31	301.34	0.56
E10		11.96	1.50	325	32.15	401.12	0.59
E11		15.92	1.99	360	35.62	500.64	0.61
E12		24.00	3.00	390	38.59	703.72	0.62
E13		32.00	4.00	414	40.96	904.78	0.63
E14		39.97	5.00	419	41.45	1105.09	0.62
E15		47.98	6.00	420	41.55	1306.40	0.62
E16		55.91	6.99	428	42.34	1505.70	0.62
E17		63.94	7.99	425	42.05	1707.52	0.61
E18	10.00	9.99	1.00	277	27.41	470.92	0.45
E19		15.02	1.50	330	32.65	628.95	0.48
E20		20.00	2.00	359	35.52	785.40	0.49
E21		29.91	2.99	390	38.59	1096.73	0.49
E22		40.00	4.00	404	39.97	1413.72	0.49
E23		49.98	5.00	410	40.56	1727.25	0.49
E24		59.90	5.99	414	40.96	2038.89	0.49
E25		69.86	6.99	418	41.36	2351.80	0.48
E26		80.02	8.00	416	41.16	2670.98	0.48
E27	12.00	12.04	1.00	307	30.37	680.09	0.41
E28		18.03	1.50	357	35.32	905.91	0.43
E29		24.02	2.00	378	37.40	1131.73	0.43
E30		36.05	3.00	410	40.56	1585.25	0.43
E31		48.00	4.00	430	42.54	2035.75	0.44
E32		59.95	5.00	437	43.24	2486.26	0.43
E33		71.99	6.00	442	43.73	2940.15	0.43
E34		83.93	6.99	444	43.93	3390.28	0.43
E35		96.12	8.01	442	43.73	3849.83	0.42
E36	14.00	14.01	1.00	310	30.67	924.07	0.36
E37		27.90	1.99	396	39.18	1534.98	0.38
E38		41.94	3.00	414	40.96	2152.49	0.37
E39		55.99	4.00	432	42.74	2770.44	0.38
E40		69.93	5.00	439	43.43	3383.56	0.37
E41		83.90	5.99	444	43.93	3997.99	0.37
E42		97.90	6.99	442	43.73	4613.74	0.37